Catalytic performance of zinc-supported copper and nickel catalysts in the glycerol hydrogenolysis

R.J. Chimentão[*1§], B.C. Miranda[2§], D. Ruiz[1], F. Gispert-Guirado[3], F. Medina[4], J. Llorca[5], J.B.O. Santos[6]*

[1] *Physical Chemistry Department, Faculty of Chemical Science, University of Concepcion, Casilla 160-C, Concepcion, Chile*

[2] *Chemical Engineering School, Universidad de Costa Rica, San Jose 2060, Costa Rica*

[3] *Scientific Resources Service Universitat Rovira i Virgili, Tarragona 43007, Spain*

[4]*Department of Chemical Engineering, Universitat Rovira i Virgili, Tarragona 43007, Spain*

[5]*Institute of Energy Technologies, Department of Chemical Engineering and Barcelona Research Center in Multiscale Science and Engineering, Universitat Politècnica de Catalunya, EEBE, 08019 Barcelona, Spain*

[6] *Department of Chemical Engineering, Universidade Federal de São Carlos (UFSCAR), São Carlos, Brazil*

§ These authors contributed equally

* Corresponding author: rchimenton@udec.cl (R.J. Chimentão)

Phone number: +56 (041) 220-3354

Abstract

Gas-phase catalytic conversion of glycerol to value added chemicals was investigated over zinc-supported copper and nickel catalysts. The addition of aluminum in the support was also investigated in glycerol conversion and the results indicate an increase in the acidity and adsorption capacity for both copper and nickel catalysts. HRTEM and XRD analysis revealed NiZn alloy formation in the Ni/ZnO catalyst. The XRD patterns of the prepared ZnAl mixed oxide catalysts show the presence of Gahanite phase ($ZnAl_2O_4$). In addition, H_2 chemisorption and TPR results suggest a strong metal-support interactions (SMSI) effect between Ni and ZnO particles. Bare supports ZnO and ZnAl (Zn/Al=0.5) were investigated in the glycerol conversion and they did not presented activity. Copper supported on ZnO and ZnAl mixed oxide (Zn/Al=0.5) was active towards hydroxyacetone formation. Nickel was active in the hydrogenolysis of glycerol both for C–C and C–O bonds cleavage of glycerol producing CH_4. Strong metal-support interaction (SMSI) between Ni and ZnO has a remarkable suppression effect on the methanation activity during the glycerol conversion.

Key-words: *glycerol, hydrogenolysis, dehydration, hydroxyacetone, copper, nickel, catalyst*

1. Introduction

Glycerol is the common constituent of all fat and oil molecules, and it is produced in large quantities as a side product in oleochemical and biodiesel industries [1]. Glycerol is one of the top 12 building block chemicals that can be converted to value-added products [2]. In the last years clean and renewable alternative chemical routes for glycerol valorization have been developed [3, 4].

Glycerol hydrogenolysis have been performed under hydrogen pressure both in gas and liquid phase and in the presence of metallic catalysts [5, 6], leading to formation of 1,2 propanediol (1,2-PDO), 1,3-propanediol (1,3-PDO), and ethylene glycol (EG) [7-9]. Glycerol conversion has been studied in the presence of different metallic, bimetallic and mixed oxide catalysts [10-12]. Noble metals such as Ru [13, 14], Rh [15, 16], Pt [17, 18] have been explored for the hydrogenolysis of glycerol. Although the noble metal catalysts are effective for the hydrogenolysis of glycerol at a relatively low temperature, the high cost and lower selectivity do not fit with industrial application requirements.

Generally, a catalyst with both dehydration and hydrogenation ability is required for glycerol transformation to value-added compounds [19]. The conversion of the oversupplied glycerol to high-valued hydroxyacetone is of potential application in chemical, food, and cosmetics industries [20]. Previous work reported that transition metals not only work as a hydrogenation catalyst, but they are also involve in the glycerol dehydration into hydroxyacetone [21]. Hydroxyacetone can be formed via direct dehydration of glycerol and subsequent keto-enol tautomerization [22]. Dehydration of glycerol to hydroxyacetone follows a reaction pathway involving either direct dehydration of primary hydroxyl-group or dehydrogenation followed by dehydration [23]. In addition, hydroxyacetone is an intermediate in the formation of 1,2-PDO and this product is used for the synthesis of resins, liquid detergents, cosmetics and chemical process fluids [5]. 1,2-PDO is currently produced by the hydration of propylene oxide. Because propylene oxide is produced from fossil resources, the production of hydroxyacetone from bio-derived glycerol is very attractive [24].

Cu based catalysts are efficient to promote selective glycerol conversion to hydroxyacetone. It is widely accepted that Cu-based catalysts are known for the lower ability to cleave the C-C bonds of a glycerol molecule resulting in a less undesired degradation products.[2]. Copper-supported catalysts have been employed in glycerol hydrogenolysis reaction [25]. It is proposed that Cu metallic site is involved in the dehydrogenation of glycerol to glyceraldehyde, followed by its dehydration and subsequent hydrogenation to hydroxyacetone [26]. In most cases, the metallic copper is combined to acid-basic supports and these bifunctional catalytic systems are reported to be efficient as well in N_2 or H_2 atmosphere in the selective dehydration of glycerol to hydroxyacetone [27].

Nickel-based catalysts are interesting materials since Ni is inexpensive and has the capability to break the C-C bond efficiently leading to formation of ethylene glycol (EG). [20, 28, 29]. EG is one of the basic raw materials for chemical fiber. Huang *et al.* [30] reported that Ni/Al_2O_3 showed high selectivity to CH_4 during vapor phase glycerol hydrogenolysis in a fixed bed reactor. Perosa *et. al.* [31] reported 97% glycerol conversion and demonstrated that Raney Ni catalyst was an active and efficient catalyst for glycerol hydrogenolysis to produce glycols at 190 ^{0}C. Raney Ni catalyst for production of ethylene glycol without external hydrogen donation was proposed by previous work [32]. Ueda et al. [33] prepared a Ni/γ-Al_2O_3 catalyst promoted by a small amount of Pt which showed a high selectivity for ethylene glycol from glycerol hydrogenolysis.

The nature of the support [34] is important in the hydroxyacetone production. A variety of supports have been evaluated in the glycerol dehydration such as metal phosphates [35],

metal oxides [36], zirconia based materials [37], zeolites [38], heteropolyacids [39] and binary mixtures of zinc oxide, tin oxide, zirconia, titania, alumina and silica [40]. Acidic supports promote the dehydration step to yield hydroxyacetone from glycerol. On Lewis acid sites glycerol is selectively dehydrated to hydroxyacetone, while in Brönsted acid sites glycerol is converted to acrolein [41]. The dehydration of vicinal diols results in an enol. This readily tautomerizes into a keton or aldehyde which is subsequently hydrogenated. The keto-enol tautomerization stabilizes the system, which makes the dehydration of diols relatively easy. Lewis acid sites can coordinate more easily to primary alcohols, thereby weakening the C-O bond [42]. Additionally, activity of copper and nickel-based catalysts can be improved supporting it in mixed oxides which are usually synthesized by co-precipitation or impregnation methods. Catalysts containing mixed metal oxides have been found to be more active than individual component [43]. Supported nickel-based catalysts are the most often used in methanation reactions. Interactions between metal nanoparticles and support materials can strongly influence the catalytic performance. Previous works [44] revealed that strong metal-support interactions (SMSI) between Ni and ZnO have suppression effect on the methanation activity. Strong metal-support interactions between Ni and ZnO particles can provides a way to modulate the methanation performance of Ni/ZnO on the valorization of biomass derived compounds to value-added products. In those cases, the methanation function of nickel-based catalysts can be undesired and it is very meaningful for improving nickel based catalytic properties and expanding their application fields.

In the present work we have studied the glycerol conversion catalyzed by non-noble metals catalysts such as Cu and Ni supported over zinc oxide (ZnO) and zinc aluminum oxide (with

Zn/Al molar ratio of 0.5). The chemical properties of the metal employed and the support nature on the catalytic performance have been studied.

2. Experimental

2.1 Catalyst preparation

The ZnO and ZnAl mixed oxide with molar ratio of Zn/Al = 0.5 were prepared by co-precipitation method using a salt aqueous solution of 150 cm^3 of deionized water with $Zn(NO_3)_2.6H_2O$ and/or $Al(NO_3)_3.9H_2O$ with correspondent appropriated quantities. The correspondent salt aqueous solution was added drop wise into a glass vessel initially containing 200 cm^3 of deionized water. The pH was controlled by adding a solution containing 2 mol L^{-1} NaOH +1 mol L^{-1} Na_2CO_3 and the pH was kept at about 10 under vigorous stirring. The resultant precipitated solid was washed several times with hot deionized water, dried at 373 K for 12h and finally calcined at 673 K for 4 h. The ZnO and ZnAl supports were impregnated with 10 wt.% nickel or copper by incipient wetness impregnation with an aqueous solutions containing $Ni(NO_3)_2\times6H_2O$ or $Cu(NO_3)_2\times6H_2O$ precursors. After calcination, the samples were reduced at 723 K in a flow of hydrogen for 4 h before reaction. The samples were labeled as ZnO; ZnAl, Cu/ZnO, Cu/ZnAl, Ni/ZnO and Ni/ZnAl.

2.2 Catalyst Characterization

The specific surface areas, cumulative pore volumes and average pore diameters of the samples were measured by the BET method using N_2 adsorption/desorption at 77 K in a Quadrasorb SI, from Quantachrome Instrument. Each sample was degassed under vacuum at

393 K for 10 h. Nitrogen was used as adsorbate gas for the analysis. The BET specific surface area was calculated from the range $P/P_0 = 0.05–0.35$ in the adsorption branch while the pore size distribution was calculated from the desorption branch.

X-ray diffraction (XRD) measurements were made using a Bruker-AXS D8-Discover diffractometer with parallel incident beam (Göbel mirror) and vertical theta-theta goniometer, XYZ motorized stage mounted on an Eulerian cradle, diffracted beam Soller slits, a 0.2º receiving slit and a scintillation counter as a detector. The data were collected in the 2θ range of 5 and 70º with an angular step of 0.05º at 3s per step. Cuk radiation (1.5417 A) was obtained from a copper X-ray tube operated at 40 kV and 40 mA. Identification of the crystal phases was achieved by comparison of the XRD profile with the ICDD data base (International Centre for Diffraction Data, release 2018).

The Rietveld refinement [45] was performed with the TOPAS v5 software [46]. The background was modelized with a 3^{rd} order Chebyshev polynomial. The instrumental contribution to the diffraction profile was calculated with the Fundamental Parameters Approach [47]. The peak width of each phase was modelled with the Double-Voigt Approach [48] by considering only the Lorentzian contribution of the crystallite size effect and discarding any contribution of the microstrain to the peak width. The averaged integral breadth was obtained from the resulting fitted Voigt function to the whole diffractogram. The Scherrer equation [49] was then applied to obtain the apparent crystallite size. The percentage of each phase were estimated from the well-known formulas from the refined Rietveld scale factor [50].

Autochem II 2920 was used for determination of the adsorption capacity and percentage of dispersion of copper using N_2O chemisorption. Firstly, the copper catalyst was reduced with 5%H_2/Ar (20 mLmin^{-1}) at 5 $^{\circ}$C/min from 298 K to 673 K holding the maximum temperature for 1 h. Selective oxidation of the copper surface to Cu_2O was performed under 20%N_2O/Ar flow (20 mL min^{-1}) at 333 K ($N_2O + 2Cu_{surface} \rightarrow Cu_2O_{surface} + N_2$). Then Cu_2O surface was reduced with 5% H_2/Ar (20 mL min^{-1}) at 5 $^{\circ}$C min^{-1} from 298 K to 1173 K ($H_2 + Cu_2O_{surface} \rightarrow 2Cu_{surface} + H_2O$). Surface copper was determined considering the stoichiometry of N_2O/Cu = 0.5 mol_{N2O} mol_{Cu}^{-1} and dispersion was calculated as the ratio between the amount of copper surface and total nominal copper content.

The chemisorption analysis of nickel samples was performed in a Micromeritrics ASAP 2020 instrument by double isotherm method. The hydrogen adsorption capacity was calculated assuming spherical particles and stoichiometric factor H/Ni=1 (atomic chemisorbed hydrogen per surface of nickel atoms). Nickel catalyst was treated in He flow at 400 K for 1 h. The nickel sample was reduced for 2 h at 623 K and subsequently out-gassed for 30 min. Finally nickel sample was cooled to 310 K and evacuated at 310 K for 30 minutes. The hydrogen adsorption isotherm was recorded at 310 K.

Temperature programmed reduction was carried out with 5% H_2/Ar (20 ml/min) at 5 $^{\circ}$C min^{-1} from 298 K to 1173 K in an Autochem II 2920. The hydrogen consumption was monitored with a TCD detector. Water was trapped in ice/water/salt bath in a Dewar.

The total quantity of acid sites was determined by temperature programmed desorption of NH_3 in Autochem II 2920. The sample was pretreated with Ar at 353 K during 1 h and then cooled to room temperature and treated with NH_3 flow. The desorption of NH_3 was measured by heating the sample from room temperature to 1173 K at a heating rate of 5 $^{\circ}C\ min^{-1}$ in He flow. Water was trapped in ice/water/salt bath in a Dewar device.

The microscope used for high-angle annular dark-field scanning transmission electron microscopy (HAADF-STEM), high-resolution (HRTEM) and for analysis of Energy Dispersive Spectroscopy (EDS) was a FEI Tecnai F20 equipped with a field emission electron gun and operating at 200 kV. The samples were dispersed in an alcohol suspension and a drop of the suspension was placed over a grid with holey-carbon film.

2.3 Glycerol reaction

Gas phase glycerol reaction was carried out in a quartz fixed bed down flow reactor. The reaction was conducted during 5 h using 100 mg of catalyst, at atmospheric pressure and at 573 K. An aqueous solution of glycerol (3 v/v%) was pumped by a syringe pump with a flow of 3.5 mL h^{-1} and it was mixed with 5%H_2/Ar and injected together into the reactor.

The condensed products were analyzed by HPLC equipped with an ICSep ICE-COREGEL 87H3 Column and DAD and RID detectors. The mobile phase was deionized water with pH controlled to 2.2 by addition of sulfuric acid. The flow of the mobile phase was of 0.6 mL min^{-1} and a pressure of 5 MPa. The temperature of the HPLC column was 313 K and 50 min of analysis for each chromatogram. The gaseous products were analyzed by an on-line gas chromatograph equipped with a HP-Plot Q column (polystyrene-divinylbenzene stationary phase, 30 m×0.32 mm×20 μm) and a FID detector.

The glycerol conversion and the selectivity based on carbon to each product was defined as:

$$Conversion\ of\ glycerol\ (\%) = \frac{Moles\ of\ glycerol\ reacted}{Initial\ moles\ of\ glycerol} x100$$

$$Selectivity\ (\%) = \frac{Moles\ of\ carbon\ in\ specific\ product}{Moles\ of\ carbon\ in\ all\ products} x100$$

3. Results and Discussion

3.1 Catalyst Characterization

Figure 1 shows the XRD patterns of the calcined supports and reduced copper and nickel catalysts. The phases identified in the ZnO support sample (Figure 1a) correspond to Zincite (ICDD card 36-1451; space group *$P6_3mc$* with lattice constants: a = 3.24982 Å and c = 5.2066 Å). It is known that under ambient conditions the thermodynamically stable phase of zinc oxide is zincite that crystallizes in the hexagonal *wurtzite* structure type [51]. Additional peaks were observed for the sample Ni/ZnO which belongs to the structure of NiZn alloy (ICDD card 6-672, space group I4/mmm, lattice constants: a = 2.759 Å and c = 3.220 Å). There are not evidences of the presence of metallic Ni in this sample. XRD pattern for Cu/ZnO sample exhibits, in addition to zincite, a set of broad peaks that has been interpreted as an overlap of two phases: peaks of metallic copper (ICDD card 4-836, space group Fm-3m, lattice constants: a = 3.6150 Å) and peaks produced by α-brass (Cu_xZn_{1-x} $0<x<0.6$) ($Cu_{0.64}Zn_{0.36}$, ICDD card 50-1333, space group Fm-3m, lattice constants: a = 3.6961 Å). The approximate composition of the α-brass was estimated from the refined cell parameter by fitting the XRD pattern with the Rietveld method and applying the Vegard's law [52]. The cell parameter dependence of the α-brass structure with the Zn content was calculated from

individual entries of the Pearson's Crystal Data database. Percentage estimated for each phase and its crystallite size from the XRD pattern for the samples are presented in Table 1.

XRD diffractogram (Figure 1b) recorded for ZnAl support shows only the presence of diffraction peaks attributed to the gahnite ($ZnAl_2O_4$) (ICDD card 5-669, space group Fd-3m, lattice constants: a = 8.0848 Å) that corresponds to the zinc spinel. In addition, no peaks corresponding to alumina crystal phase were observed. Additional peak attributed to metallic nickel or other nickel species were not observed for Ni/ZnAl sample. However, in the case of Cu/ZnAl sample two low intensity peaks at $2\theta = 43^0$ and 50^0 were interpreted as a mixture of metallic copper phase and α-brass, in the same way that was interpreted the diffractogram for Cu/ZnO sample.

Specific surface areas of the samples are reported in Table 2. Nitrogen adsorption-desorption isotherm of ZnO at 77 K exhibit a characteristic of as non-porous nature with the absence of a hysteresis loop, small values of specific pore volume (0.013 cm^3/g), and the specific surface area (S_{BET} = 6 m^2/g). This suggests that S_{BET} of ZnO is probably derived from the outer surface of the non-porous particles in agreement with conclusion drawn elsewhere [53]. It must be added that ZnO presents a hysteresis loop that can be classified as a Type II. The overlapped adsorption-desorption curves were found at lower pressure for both copper and nickel supported on ZnO material. Simultaneously, at high pressure, hysteresis loops for Cu/ZnO and Ni/ZnO are narrower than those observed for ZnAl supported catalysts (Figure 2).

On the other hand, ZnAl based materials are mesoporous materials based on the N_2 adsorption-desorption showing an isotherm of Type IV. Its hysteresis loops are Type H3 indicating slip-shaped pores. The surface area of ZnAl sample is 128 m^2/g. Aluminum species may act as textural promoter in the resultant mixed oxide ZnAl material. The addition of aluminum may lead to nanocrystals of the resultant ZnAl mixed oxide material (gahnite phase) when compared with ZnO material (zincite phase). Specific surface areas of ZnAl supports in general decreased after impregnation with copper or nickel precursors suggesting partial blockage of the porous structure of the supports. The decrease in textural properties can be attributed to a partial collapse of aggregate structures of the support by the introduction of metal species. The same tendency was observed to the corresponding pore volume and pore size. In the case of ZnO support, the introduction of nickel species resulted in a material with higher specific surface area compared with pure ZnO. This is probably caused by an interface reaction between Ni and ZnO to generate NiZn alloy. Bulk NiZn alloy may be formed by the spill-over of atomic hydrogen from the Ni metal to the ZnO, leading to facile reduction of the ZnO and the migration of Zn to the metallic surface [54].

The chemisorption capacity of Cu and Ni samples is shown in Table 2. Cu/ZnO presented a chemisorption capacity of 374 μmol/g_{cat} whereas for Cu/ZnAl was noticed a value of 570 μmol/g_{cat}. Ni/ZnO and Ni/ZnAl presented an adsorption capacity of 4 μmol/g_{cat} and 44 μmol/g_{cat} respectively. The presence of aluminum species markedly increases the adsorption capacity of both Cu and Ni catalysts. H_2 chemisorption experiments show evidences for strong metal-support interactions (SMSI) effect between Ni and ZnO particles. SMSI diminished the H_2 capacity of Ni/ZnO compared with Ni/ZnAl sample (Table 2).

TPR profiles of the supports and freshly calcined catalysts are shown in Figure 3. TPR profiles for ZnO and ZnAl did not indicate H_2 consumption at the temperature range studied. It must be added that previous work reported a very weak H_2 consumption during the reduction caused by the reaction of hydrogen and oxygen atoms partially released from ZnO lattices [55]. The TPR profile for the Ni/ZnO sample presents a reduction peak at about 630 K and a broad peak above 700 K. The first peak can be attributed to the reduction of NiO particles with weak interaction with the support while the second broad peak can be due to reduction of NiO particles with strong interaction with ZnO [33]. Wang et. al. [44] reported that the H_2 consumption peak above 700 K is caused by the interfacial interaction between Ni and ZnO generating NiZn alloy although metallic nickel phase was not identified by XRD. At least two reduction stages are observed in the TPR of Ni/ZnAl sample. The first one, situated in the temperature range 525-760 K is associated with NiO surface species reduction [56]. Based on the TPR profiles of Ni/ZnO and Ni/ZnAl samples (Figure 3), the peak attributed to strong Ni and ZnO interactions changes with the presence of aluminum. This fact suggests that Al species are involved in binding the supported Ni species. This feature is in agreement with previous research reported elsewhere [57]. The presence of Al_2O_3 may weaken the interaction of Ni species and ZnO indicating that the mixed oxide supported Ni catalyst may facilitate the reducibility in agreement with previous work [58]. Cu/ZnO presents at least two reduction peaks observed at about 468 K and 502 K which correspond to copper oxides reduction ($CuO \rightarrow Cu_2O \rightarrow Cu$) [59]. Shishido *et al.* [60] have reported the presence of Cu^+ together with Cu^0 on the reduced Cu/ZnO and $Cu/ZnO/Al_2O_3$. Formation of dilute alloy of zinc in copper (α-brass) cannot be ruled out during the catalyst reduction since

α-brass was estimated from the refined cell parameter by fitting the XRD pattern with the Rietveld method. Reduction of Cu species supported on ZnAl mixed oxide is favored compared with Cu/ZnO material. TPR profile of Cu/ZnAl consists of at least two overlapping peaks in the range of 380 to 520 K. The onset of reduction is apparent at about 388 K. At about 436 K H_2 consumption increases rapidly, reaching a maximum at 482 K. Higher temperature reduction effect observed in the case of copper supported on the binary oxide (ZnAl) is attributed with $CuAl_2O_4$ structure reduction although this phase was not visible in the XRD recorded for Cu/ZnAl sample. Turco *et al.* [61] also confirmed easy reduction of Cu^{+2} to Cu^{+} and Cu^{0} in the case of $CuO/ZnO/Al_2O_3$ catalyst.

NH_3-TPD was carried out to determine the acidity of the catalysts and the results are presented in Figure 4. The strength of the acid sites can be classified in weak (<473 K), moderate (473-723 K) and strong (>723 K) [62]. Ni/ZnO sample shows a desorption peak in the range of 440 to 600 K while the Ni/ZnAl sample shows a broad shoulder in the temperature range of 350 to 700 K. The NH_3-TPD profiles show that moderate acid sites are present in the Ni/ZnO sample while weak and moderate acid sites are observed in the Ni/ZnAl sample. The presence of aluminum predominantly increases the weak acid sites as observed for Ni/ZnAl sample in the NH_3 desorption peak at about 473 K. Previous work [57] observed an increase in the quantity of acid sites due to the surface hydroxyl ions of Al_2O_3 when it was combined with ZnO. The introduction of aluminum species increases the total acidity in all samples as shown in Table 2. Nickel catalysts present a higher quantity of total acid sites compared with the copper samples. The same aluminum effect is drawn in the Cu/ZnO and Cu/ZnAl samples.

Figures 5 and 6 show HAADF-STEM images of the Ni/ZnO sample. It can be seen the occurrence of two distinct phases, namely rounded nanoparticles with high brightness supported over less bright support particles. Since HAADF-STEM is sensible to the atomic weight of the elements, the brighter particles likely contain Ni. These nanoparticles are very well distributed over the support with narrow size distribution (5-15 nm) (Figure 5). The area enclosed in the white square in Figure 6a is shown at higher magnification in Figure 6b. The Ni nanoparticles are in tight contact with the support, suggesting a strong interaction. The areas enclosed inside the white squares in Figure 6b are shown in HRTEM mode in Figures 6c and 6d. The insets correspond to FT images obtained from selected areas corresponding to the nanoparticle shown in the image (NiZn alloy) and the support (ZnO). Figure 6c shows that spots at 2.09 Å and 1.94 Å match perfectly with the (101) and (110) crystallographic planes of the NiZn alloy. On the other hand, spots at 2.60 Å and 1.91 Å correspond to the (002) and (102) crystallographic planes of ZnO. No epitaxial relationship is observed. A similar analysis is shown in Figure 6d, where a good contact between the NiZn alloy nanoparticle and the support is again evidenced. Another representative HRTEM image of the Ni/ZnO sample is shown in Figure 7a. Again, no epitaxial relationship exists between the NiZn alloy nanoparticle and the ZnO support. Figure 7b shows a NiZn nanoparticle well anchored onto ZnO, but without epitaxy. Both phases are totally crystalline. Figure 7c corresponds to a line profile analysis of Ni, Zn and O carried out with EDX along the yellow line. It is clear that Ni is encountered solely in the nanoparticles, whereas Zn is present both in the nanoparticles and in the support, in accordance to the HRTEM results outlined above. Finally, Figure 7d shows an EDX mapping of Ni and Zn where the correspondence between Ni and Zn species is evident (green color: Ni species and red color: Zn species).

Figures 8a and 8b show low-magnification images recorded in bright-field and HAADF-STEM of the Ni/ZnAl sample, respectively. The morphology of the sample at the nanoscale is totally different from that of Ni/ZnO discussed above. The sample is comprised by individual particles below ca. 6 nm in size. Another bright-field TEM image is depicted in Figure 9a. In addition to these particles, in some regions of the sample there are some large particles (up to 50-60 nm) with a platelet morphology in addition to the small ones. These are shown in Figure 9b in HAADF-STEM and Figure 9c in bright field. Given their lower electron contrast, these larger platelets likely correspond to alumina particles. HRTEM images are shown in Figure 10a and Figure 10b. The FT image of Figure 10a shows spots at 2.86 Å, which corresponds well to the (220) crystallographic planes of $ZnAl_2O_4$. These lattice fringes are identified through the entire HRTEM image, as indicated. In addition, some lattice fringes at 2.80 Å are also identified, which corresponds to the (220) crystallographic planes of Al_2O_3. The size of the $ZnAl_2O_4$ crystallites is mostly between 3 and 6 nm. The alumina platelets are comprised by crystalline nanodomains below ca. 4 nm. The small size of the alumina nanodomains and their low occurrence account for the absence of alumina peaks in the XRD pattern of this sample. Similarly, in the HRTEM image reported in Figure 10b numerous $ZnAl_2O_4$ crystallites are identified. The FT image of one of them (enclosed by a dashed rectangle in the lower part of the image) shows spots at 2.4 and 2.9 Å, which correspond to the (311) and (220) crystallographic planes of $ZnAl_2O_4$, respectively. In addition to $ZnAl_2O_4$, the image also shows the occurrence of Ni nanoparticles with size of about 2-3 nm. One of them is shown in the inset (upper part); the lattice fringes at 2.0 Å correspond to the (111) crystallographic planes of Ni. It has been not possible to perform EDX analyses in individual particles due to their small size and to drift during acquisition.

3.2 Glycerol conversion

Glycerol transformation using only supports (ZnO or ZnAl) as catalysts resulted in negligible conversion of glycerol. Glycerol conversion for Ni/ZnAl (Figure 11a) shows almost only CH_4 as product. The observed formation of CH_4 is mainly because of the strong C-C bond breaking capacity of nickel catalyst [20, 28, 29]. On the other hand, the main products obtained in the conversion of glycerol over Ni/ZnO sample after 4h of reaction were hydroxyacetone, acetaldehyde, ethylene glycol, lactide and CH_4 (Figure 11b). As the reaction progressed, the CH_4 decreased and started to appear products derived from the dehydration route (Figure 11b). For Ni/ZnO catalyst lactide, hydroxyacetone, pyruvaldehyde, CH_4, acetaldehyde and ethylene glycol were the main products obtained at 4 h of reaction exhibiting respectively selectivity values at about 37%, 16%, 13%, 20%, 12% and 2%

The addition of Al_2O_3 into ZnO changed the products formed on Ni during glycerol conversion. It has been reported previously that SMSI exhibits a suppression effect on the methanation activity on Ni/ZnO catalyst [44]. Here, HRTEM confirms the strong interaction of the Ni nanoparticles with the ZnO support (Figures 5 and 6). The most important signature of the SMSI effect is the remarkable inhibition of chemisorption capacity for H_2 (Table 2) probably due to changes in physical and chemical properties of metal particles promoted by NiZn alloy formation in the Ni/ZnO sample. Based on the results of Table 2, the amount of H_2 chemisorbed on the Ni/ZnO sample is about 12 $\mu mol g_{cat}^{-1}$ while Ni/ZnAl is 37 $\mu mol\ g_{cat}^{-1}$. Only the fraction of available metallic nickel must be engaged with the observed hydrogen chemisorption in the Ni/ZnO sample. The inhibition of chemisorption capacity for H_2 in the

Ni/ZnO catalyst was mirrored in the inhibition in the selectivity of CH_4 during the glycerol conversion (Figure 11b). Copper species on ZnAl and ZnO (Figures 11c and 11d, respectively) favor the glycerol dehydration route. The main products formed for Cu-based catalysts were hydroxyacetone and lactide. At 4 h of reaction Cu/ZnAl sample exhibits at about 40% of selectivity to hydroxyacetone. Cu/ZnAl sample presented higher total acidity than Cu/ZnO sample with total quantity of acidy sites of 131 $\mu mol/g_{cat}$ (Table 2). Acidity may induce the dehydration of glycerol to hydroxyacetone on copper-based catalyst. Dehydration of glycerol catalyzed by acids occurs either in gas or liquid phase as pointed out by previous work [63].

The metal oxide supports may facilitates copper to be more active for the polarization of glycerol molecule. Mane et al. [23] reported a detailed study on the mechanism of liquid-phase glycerol dehydration into hydroxyacetone over Cu supported catalysts. They concluded that glycerol dehydration to hydroxyacetone is not only catalyzed by acid sites but also by metallic Cu. D. Sun et al. [21] have also reported that transition metals such as Pt, Ru, and Cu do not only work as a hydrogenation catalyst, but also are involved in the glycerol dehydration to hydroxyacetone. Copper-based catalyst is particularly selective towards C-O bond cleavage. It has been suggested that the acid sites participate in the activation of glycerol [64]. Previous work [65] has reported that Raney Cu gave 86% selectivity to 1,2-PDO with a conversion at about 80% at 240 ^0C and a H_2 pressure of 30 atm. This may indicate that transition metals such as Cu solely provide the active sites to catalyze the liquid phase dehydration of glycerol into hydroxyacetone. Previous work [66] performed DFT

calculations and demonstrated that Lewis acid sites of Al_2O_3 support may facilitates transition metals in the glycerol adsorption.

It is reasonable to assume that the total acidity and adsorption capacity play vital role on the glycerol conversion. Cu and Ni adsorption capacity were enhanced in the ZnAl support compared with ZnO support promoting the glycerol conversion. Based on Figure 12 at 4h of reaction a conversion of 40% was noticed for Ni/ZnO whereas a conversion of 100% was observed for Ni/ZnAl. On the other hand, at 4 h of reaction a conversion of 30% was observed for Cu/ZnO and 50% for Cu/ZnAl. Cu/ZnO, Cu/ZnAl and Ni/ZnAl generated dehydration products such as hydroxyacetone and lactide. Considering the results at 60% of conversion it is observed a yield of 22% of lactide for Ni/ZnO. A yield of 29% and 26% of hydroxyacetone was observed for Cu/ZnAl and Cu/ZnO respectively. On the other hand, almost total methanation was observed for Ni/ZnAl catalyst. It appears that there is some inhibition of the active nickel sites for methanation by the formation of NiZn alloy.

Deactivation remained the major drawback in the materials investigated in the present work. Previous work has attributed that the nature of the carbonaceous deposition is due to the formation of heavy polycondensated and cyclic compounds promoted by acid sites [67]. The formation of carbon deposits during dehydration reaction of glycerol may result from consecutive reactions of glycerol, like oligomerization on acid catalyst surface sites and or side reactions such as aldol condensation of carbonyl compounds [40]. It must be added that partial oxidation of the metal species due to the aqueous medium may also contribute to some deactivation observed. The water in aqueous solution of glycerol may oxidize copper and nickel particles in the first hours of the reaction contributing to the observed deactivation as

shown Figure 12. It must be also considered that the support surface also may suffer hydroxylation by both the water generated in the reaction and that already present in the reaction medium. The water content may reduce the number of active sites contributing to the observed deactivation.

3.3 General reaction route

The conversion of glycerol in the presence of hydrogen can occur via several pathways as reported [21]. Glycerol can be transformed directly via hydrogenolysis to form diols. The subsequent diols can undergo further hydrogenolysis to form primary alcohols and methane. In addition, glycerol can also suffer dehydration producing hydroxyacetone or acrolein. Side reactions, such as oligomerization, dehydrogenation, hydrogenation must be taken in account to understand the product selectivity [67].

Previous works have reported reaction routes for glycerol dehydration over solid acid catalysts [68-70]. It has been proposed that the terminal hydroxyl group of glycerol interacts with Lewis acid sites. This leads to the formation of an enol intermediate that rapidly rearranges to give hydroxyacetone. For Cu supported on acidic supports, hydroxyacetone is generally accepted as intermediate. In this work the main products obtained for the copper-based catalysts were hydroxyacetone, pyruvaldehyde, lactic acid and lactide. Glycerol was converted to hydroxyacetone by dehydration. Pyruvaldehyde is formed from dehydrogenation of hydroxyacetone. Pyruvaldehyde can be converted to lactic acid via Cannizzaro reaction. Lactide can be finally formed by dimerization of lactic acid. Methane and acetaldehyde were also observed. Methane and acetaldehyde can be formed directly from the hydrogenolysis of glycerol. Concerning Ni supported catalyst C-C bond cleavage route

to the formation of CH_4 is the mainly one on Ni/ZnAl catalyst. For Ni/ZnO sample it is noticed that strong metal-support interactions between Ni and ZnO particles alters the catalytic properties significantly suppressing the methane formation. This suggests that dehydration and dehydrogenation routes can occur on NiZn alloy system while hydrogenolysis is favored on metallic Ni species. Based on the product distribution, a possible reaction pathway based on the catalysts investigated in the present study is illustrated in Scheme 1.

4. Conclusions

Acidity and adsorption capacity play vital role in glycerol conversion. It is reasonable to consider that the acidity of ZnO and ZnAl promotes activity. The presence of aluminum in the support increases the acidity and adsorption capacity for both copper and nickel catalysts. Nickel catalyst promotes the formation of CH_4 during glycerol conversion. On the contrary, copper promotes the dehydration route of glycerol towards hydroxyacetone. Strong interaction between Ni and ZnO effectively inhibited the pathway for methanation. At 60% conversion it is observed a yield of 22% of lactide for Ni/ZnO. On the other hand, at 60% of conversion,º a yield of 29% and 26% of hydroxyacetone was observed for Cu/ZnAl and Cu/ZnO, respectively.

Acknowledgements

The authors gratefully acknowledge financial support from Fondecyt. R. J. Chimentão is grateful to Fondecyt 1180243. D. Ruiz is grateful to Fondecyt 1161660. B.C. Miranda gratefully acknowledges the Universitat Rovira i Virgili and Universidad de Costa Rica for

the financial support. J.Llorca is a Serra Húnter Fellow and is grateful to ICREA Academia program and GC 2017 SGR 128.

References

1. F. Ma and H.M. A, *Biodiesel production: a review*. Bioresour. Technol., 1999. **70**(1): p. 115.
2. E.S. Vasiliadou and A.A. Lemonidou, *Investigating the performance and deactivation behaviour of silica-supported copper catalysts in glycerol hydrogenolysis.* Appl. Catal., A, 2011. **396**: p. 177–185.
3. E. D'Hondt, et al., *Catalytic glycerol conversion into 1,2-propanediol, in absence of added hydrogen.* Chem. Commun., 2008. **45**: p. 6011–6012.
4. D. Roy, B. Subramaniam, and R.V. Chaudhari, *Aqueous phase hydrogenolysis of glycerol to 1,2-propanediol without external hydrogen addition.* Catal. Today, 2010. **156**: p. 31-37.
5. M.A. Dasari, et al., *Low-pressure hydrogenolysis of glycerol to propylene glycol.* Appl. Catal., A, 2005. **281**: p. 225-231.
6. Vasiliadou, E.S., et al., *Ru-based catalysts for glycerol hydrogenolysis—Effect of support and metal precursor*. Applied Catalysis B: Environmental, 2009. **92**(1): p. 90-99.
7. M. Pagliaro and M. Rossi, *Future of glycerol: New usages for a versatile as raw material*. 2 ed. 2010, Cambridge, UK: The Royal Society of Chemistry.
8. V.A. Goltsov, T.N. Veziroglu, and L.F. Goltsova, *Hydrogen civilization of the future—A new conception of the IAHE.* Int. J. Hydrogen Energy, 2006. **31**(2): p. 153-159.
9. G. W. Huber, S. Iborra, and A. Corma, *Synthesis of Transportation Fuels from Biomass: Chemistry, Catalysts, and Engineering.* Chem. Rev., 2006. **106**(9): p. 4044–4098.
10. J. Chaminand, et al., *Glycerol hydrogenolysis on heterogeneous catalysts.* Green Chem., 2004. **6**: p. 359–361.
11. T. Miyazawa, et al., *Glycerol conversion in the aqueous solution under hydrogen over Ru/C+an ion-exchange resin and its reaction mechanism.* J. Catal., 2006. **240**: p. 213–221.
12. X. Guo, et al., *Co/MgO catalysts for hydrogenolysis of glycerol to 1,2-propanediol.* Appl. Catal.,A, 2009. **371**: p. 108.
13. T. Miyazawa, et al., *Development of a Ru/C catalyst for glycerol hydrogenolysis in combination with an ion-exchange resin.* Appl. Catal. A, 2007. **318**: p. 244-251.
14. R. Mane, et al., *Influence of carbon based supports on selectivity behavior of diols and propanol in Ru catalyzed glycerol hydrogenolysis.* Appl. Catal. B, 2017. **204**: p. 134-146.
15. I. Furikado, et al., *Catalytic performance of Rh/SiO_2 in glycerol reaction under hydrogen.* Green Chem., 2007. **9**: p. 582-588.

16. S. Koso, Y. Nakagawa, and K. Tomishige, *Mechanism of the hydrogenolysis of ethers over silica-supported rhodium catalyst modified with rhenium oxide.* J. Catal, 2011. **280**: p. 221-229.
17. G. Shi, et al., *Effect of WOx doping into Pt/SiO2 catalysts for glycerol hydrogenolysis to 1,3 propanediol in liquid phase.* Catal. Lett., 2018. **148**(8): p. 2304–2314.
18. R. Arundhathi, et al., *Highly selective hydrogenolysis of glycerol to 1,3-propanediol over a boehmite-supported platinum/tungsten catalyst.* ChemSusChem, 2013. **6**(8): p. 1345-1347.
19. J. ten Dam and U. Hanefeld, *Renewable Chemicals: Dehydroxylation of Glycerol and Polyols.* ChemSusChem, 2011. **4**(8): p. 1017-1034.
20. S. Celerier, et al., *Glycerol dehydration to hydroxyacetone in gas phase over copper supported on magnesium oxide (hydroxide) fluoride catalysts.* Appl. Catal. A, 2018. **557**: p. 135-144.
21. D. Sun, et al., *Glycerol hydrogenolysis into useful C3 chemicals.* Appl. Catal. B, 2016. **193**: p. 75-92.
22. J. ten Dam and U. Hanefeld, *Renewable Chemicals: Dehydroxylation of Glycerol and Polyols.* ChemSusChem, 2011. **4**: p. 1017– 1034.
23. R. B. Mane, et al., *Active sites in modified copper catalysts for selective liquid phase dehydration of aqueous glycerol to acetol.* RSC adv., 2013. **3**(37): p. 16499-16508.
24. M. Besson, P. Gallezot, and C. Pinel, *Conversion of Biomass into Chemicals over Metal Catalysts.* Chem. Rev. , 2014. **114**: p. 1827-1870.
25. S. Zhu, et al., *Tailored mesoporous copper/ceria catalysts for selective hydrogenolysis of biomass-derived glycerol and sugar alcohols.* Green Chemistry, 2016. **18**: p. 782-791.
26. A. Behr, et al., *Improved utilisation of renewable resources: New important derivatives of glycerol.* Green Chem., 2008. **10**: p. 13-30.
27. T. P. Braga, et al., *Gas-phase conversion of glycerol to acetol: influence of support acidity on the catalytic stability and copper surface properties on the activity.* J. Braz. Chem. Soc., 2016. **27**: p. 2361-2371.
28. J. Tao, et al., *Kinetics of hydrogenolysis of glycerol to ethylene glycol over Raney Ni Catalyst,.* Advanced Materials Research 2014. **906**: p. 103-111.
29. R. B. Mane, et al., *Cu:Al Nano Catalyst for Selective Hydrogenolysis of Glycerol to 1,2-Propanediol.* Catal. Lett., 2010. **135**: p. 141-147.
30. L. Huang, et al., J. Chem. Technol. Biotechnol., 2008. **83**: p. 1670–1675.
31. A. Perosa and P. Tundo, *Selective Hydrogenolysis of Glycerol with Raney Nickel.* Ind. Eng. Chem. Res, 2005. **44**: p. 8535-8537.
32. A.Y. Yin, et al., *The synthesis of propylene glycol and ethylene glycol from glycerol using Raney Ni as a versatile catalyst.* Green Chem, 2009. **11**: p. 1514-1516.
33. N. Ueda, Y. Nakagawa, and K. Tomishige, *Conversion of Glycerol to Ethylene Glycol over Pt-modified Ni Catalyst.* 506-507, 2010. **39**: p. 506-507.
34. W. Oberhauser, et al., *Platinum on carbonaceous supports for glycerol hydrogenolysis: support effect.* j. Catal, 2015. **325**: p. 111-117.
35. L. R. Pizzio, C. V. Caceres, and M.N. Blanco, *Acid catalysts prepared by impregnation of tungstophosphoric acid solutions on different supports.* Appl. Catal. A, 1998. **167**: p. 283–294.

36. G. J Highfield and B.J. Moffat, *Elucidation of the mechanism of dehydration of methanol over 12-tungstophosphoric acid using infrared photoacoustic spectroscopy.* J. Catal., 1985. **95**: p. 108-119.
37. B. R. Sereshki, et al., *Reactive vaporization of crude glycerol in a fluidized bed reactor.* Ind. Eng. Chem. Res., 2010. **49**: p. 1050–1054.
38. Y. T. Kim, K. D. Jung, and E.D. Park, *Gas-phase dehydration of glycerol over ZSM-5 catalysts.* Microporous Mesoporous Mater., 2010. **131**: p. 28-36.
39. A. Martin, U. Armbruster, and A. Hanan, *Recent developments in dehydration of glycerol toward acrolein over heteropolyacids.* Eur. J. Lipid. Sci. Technol 2012. **114**: p. 10-23.
40. W.Suprun, et al., *Acidic catalysts for the dehydration of glycerol: Activity and deactivation.* J. Mol. Catal. A: Chem., 2009. **309**: p. 71-78.
41. Z. Wu, et al., *Cu/bohemite: A highly active catalyst for hydrogenolysis of glycerol to 1,2 propanediol.* Catal. Commun., 2013. **32**: p. 52-57.
42. A. Alhanash, E. F. Kozhevnikova, and I. V. Kozhevnikov, *Gas-phase dehydration of glycerol to acrolein catalysed by caesium heteropoly salt.* Appl. Catal. A: Gen., 2010. **378**(1): p. 11-18.
43. P. Mierczynski, et al., *Cu/ZnxAlyOz supported catalysts (ZnO : Al2O3 =1, 2, 4) for methanol synthesis.* Catal. Today, 2011. **176**: p. 21-27.
44. W. Wang, et al., *Strong metal-support interactions between Ni and ZnO particles and their effect on the methanation performance of Ni/ZnO.* Catal. Sci. Technol., 2017. **7**: p. 4413-4421.
45. Rietveld, H.M., *A profile refinement method for nuclear and magnetic structures.* J. Appl. Cryst., 1969. **2**: p. 65-71.
46. *TOPAS, v5.0 (Computer Software)*, in *Bruker AXS*. 2011: Karslruhe, Germany.
47. Cheary, R.W., A.A. Coelho, and J.P. Cline, *Fundamental Parameters Line Profile Fitting in Laboratory Diffractometers.* Journal of Research of the National Institute of Standards and Technology, 2004. **109**: p. 1-25.
48. Balzar, D., *Voigt-function model in diffraction line-broadening analysis.*, in *Microstructure Analysis from Diffraction*, R.L. Snyder, H.J. Bunge, and J. Fiala, Editors. 1999, International Union of Crystallography.
49. Stokes, A.R. and A.J.C. Wilson, *A method of calculating the integral breadths of Debye-Scherrer lines.* Mathematical Proceedings of the Cambridge Philosophical Society, 1942. **38**: p. 313-322.
50. Hill, R. and C. Howard, *Quantitative phase analysis from neutron powder diffraction data using the Rietveld method.* J. Appl. Crystallogr., 1987. **20**: p. 467-474.
51. A. Alkahlout, et al., *Synthesis and characterization of aluminum doped zinc oxide nanostructures via hydrothermal route.* Journal of Materials, 2014. **2014**: p. 1-8.
52. Vegard, L., *Die Konstitution der Mischkristalle und die Raumfüllung der Atome.* Zeitschrift für Physik, 1921. **5**(1): p. 17-26.
53. N. L.Finčur, et al., *Removal of alprazolam from aqueous solutions by heterogeneous photocalysts: Influencing factors, intermediates, and products.* Chem. Eng. J., 2017. **307**: p. 1105-1115.
54. Y. Suwa, et al., *Comparative study between Zn–Pd/C and Pd/ZnO catalysts for steam reforming of methanol.* Appl. Catal. A, 2004. **267**: p. 9-16.
55. Y. Lv, et al., *The surface oxygen vacancy induced visible activity and enhanced UV activity of a ZnO1−x photocatalyst* Catal. Sci. Technol., 2013. **3**: p. 3136–3146.

56. G. Chen, et al., *Hydrogen production by aqueous-phase reforming of ethylene glycol over Ni/Zn/Al derived hydrotalcite catalyst.* RSC. Adv. , 2015. **5**: p. 60128.
57. C. Weicheng, et al., *Effect of mixed oxide support for Ni/ZnO in reactive adsorption desulfurization.* China Petroleum Processing and Petrochemical Technology, 2016. **18**(4): p. 11-18.
58. M. S. Rana, et al., *Effect of support composition on hydrogenolysis of thiophene and Maya crude.* Catal. Today, 2005. **107-108**: p. 346-354.
59. L. Dussault, et al., *Microcalorimetry, TPR, XPS studies of acid-base properties of NiCuMgAl mixed oxides using LDHs as precursors,.* Thermochim. Acta, 2005. **434**(1-2): p. 93-99.
60. T. Shishido, et al., Appl. Catal. A Gen, 2006. **303**: p. 62-71.
61. M. Turco, et al., *Cu/ZnO/Al2O3 catalysts for oxidative steam reforming of methanol: The role of Cu and the dispersing oxide matrix.* Appl.Catal. B, 2007. **77**: p. 46-57.
62. J. Lif, I. Odenbrand, and M. Skoglundh, *Sintering of alumina-supported nickel particles under amination conditions: Support effects.* Appl. Catal., A, 2007. **317**: p. 62-69.
63. S. Bagheri, N. M. Julkapli, and W.A. Yehye, *Catalytic conversion of biodiesel derived raw glycerol to value added products.* Renewable and Sustainable Energy Reviews, 2015. **41**: p. 113-127.
64. D. F. Carvalho, et al., *Characterization and catalytic perfomances of copper and cobalt-exchanged hydroxyapatite in glycerol conversion for 1-hydroxyacetone production.* Appl. Catal., A, 2014. **471**: p. 39-49.
65. C. Montassier, D. Giraud, and J. Barbier, *Polyol Conversion by Liquid Phase Heterogeneous Catalysis over Metals.* Stud. Surf. Sci. Catal., 1988. **41**: p. 165-170.
66. P. Hirunsit, C. Luadthonga, and K. Faungnawakija, *Effect of alumina hydroxylation on glycerol hydrogenolysis to 1,2-propanediol over Cu/Al2O3: combined experiment and DFT investigation* RSC Adv., 2015. **5**: p. 11188-11197
67. A. S. de Oliveira, et al., *Catalytic conversion of glycerol to acrolein over modified molecular sieves: Activity and deactivation studies.* Chem. Eng. J., 2011. **168**(2): p. 765-774.
68. E. Yoda and A. Ootawa, Appl. Catal. A, 2009. **360**: p. 66-70.
69. E. Tsukuda, et al., Catal. Comm. , 2007. **8**: p. 1349-1353.
70. A. Corma, et al., *Biomass to chemicals: Catalytic conversion of glycerol/water mixtures into acrolein, reaction network.* J. Catal., 2008. **257**: p. 163-171.

Table -1 Percentage estimated for each phase and its crystallite size from the X-ray diffractograms. The values between parentheses indicate the error of the last significant digit.

Sample	phase	comp.	wt%	Crystallite Size (nm)
ZnO	Zincite	ZnO	100%	33.8 (5)
ZnAl	Gahnite	$ZnAl_2O_4$	100%	2.83 (5)
Ni/ZnO	Zincite	ZnO	86.8%	32.3 (5)
	NiZn	NiZn	13.2%	9.9 (4)
Cu/ZnO	Zincite	ZnO	90.6%	43.0 (6)
	Copper	Cu	2.2%	31 (7)
	α-brass	$Cu_{0.78}Zn_{0.22}$	7.2%	40 (4)
Ni/ZnAl	Gahnite	$ZnAl_2O_4$	100%	2.90 (5)
Cu/ZnAl	Gahnite	$ZnAl_2O_4$	96.9%	2.92 (6)
	Copper	Cu	0.9%	19 (3)
	α-brass	$Cu_{0.81}Zn_{0.19}$	2.2%	19 (3)

Table 2 – Nitrogen physisorption, NH_3-TPD and chemisorption analysis of the samples.

Sample	S_{BET} (m^2/g)	Pore volume (cm^3/g)	Pore diameter (nm)	NH_3 desorption ($\mu mol/g_{cat}$)	Chemisorption Capacity ($\mu mol/g_{cat}$)
ZnO	6	0.013	2.88	-	-
ZnAl	128	0.295	3.62	-	-
Ni/ZnO	10	0.025	11.68	682	4[a]
Cu/ZnO	4.2	0.007	6.32	131	374[b]
Ni/ZnAl	109	0.192	10.88	1790	44[a]
Cu/ZnAl	86	0.195	3.62	479	570[b]

[a] H_2 chemisorbed; [b] N_2O Chemisorbed

Figure 1

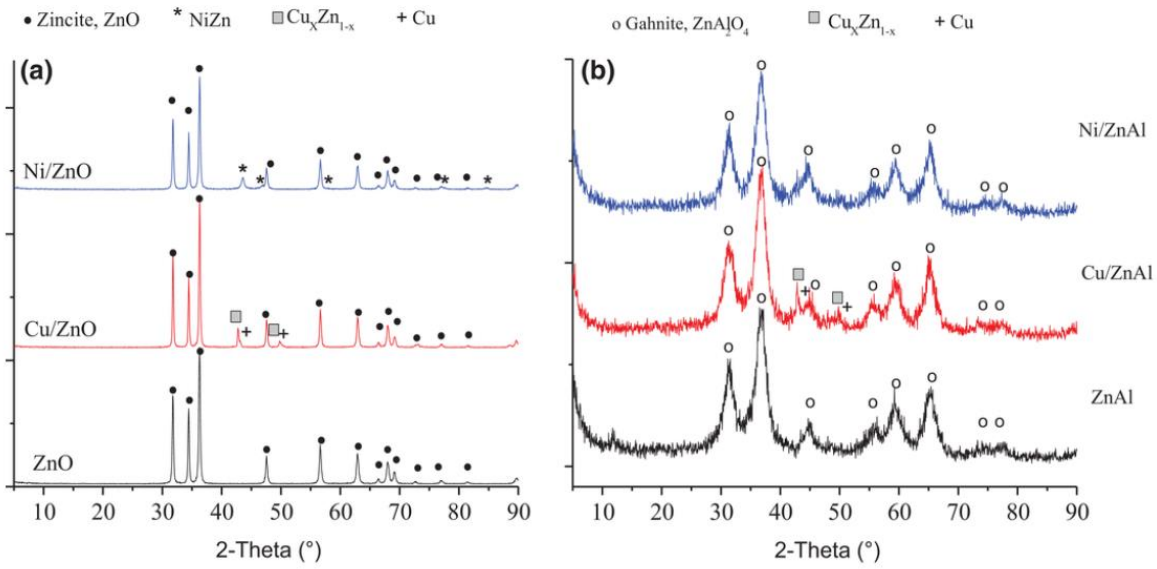

Figure 2

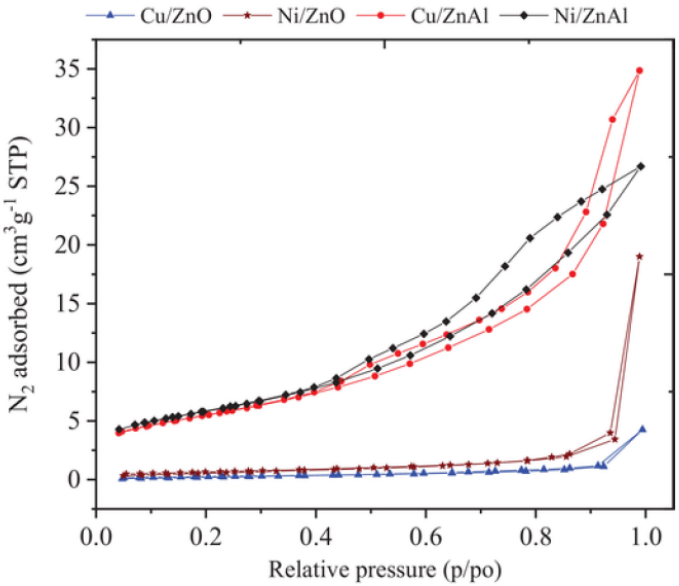

Fig. 2. N_2-physisorption for Ni and Cu samples.

Figure 3

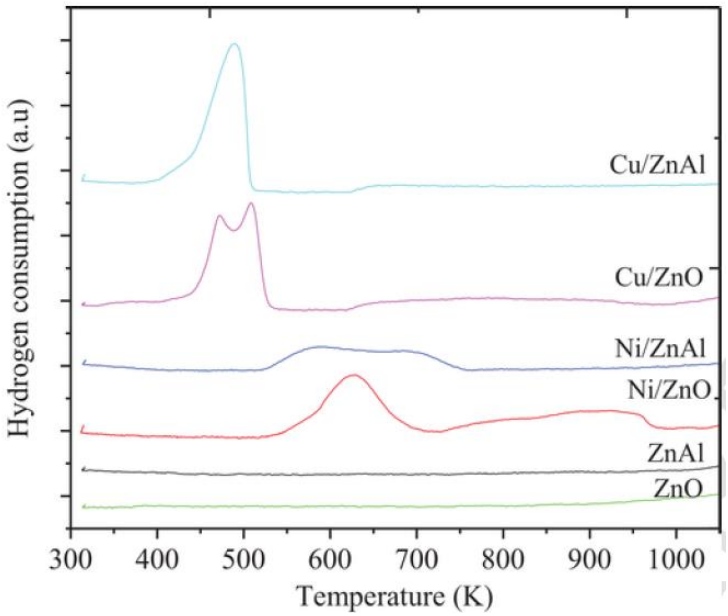

Figure 4

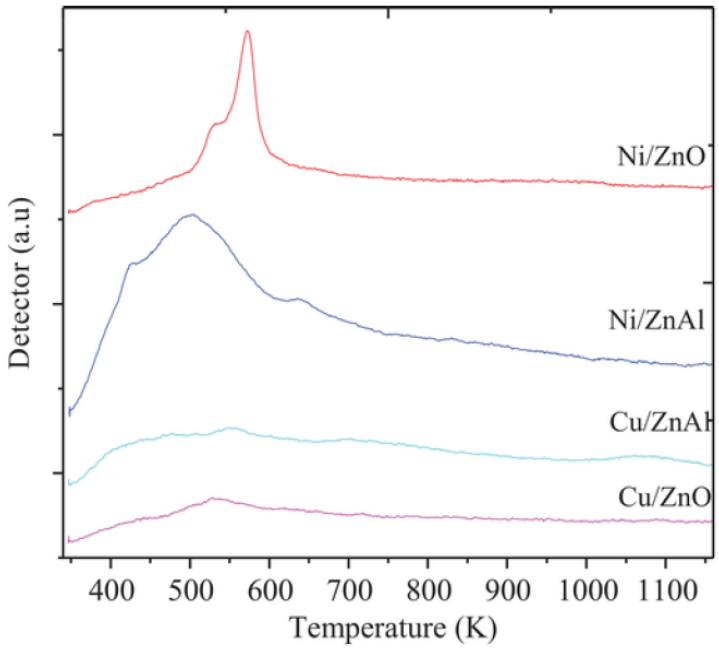

Figure 5

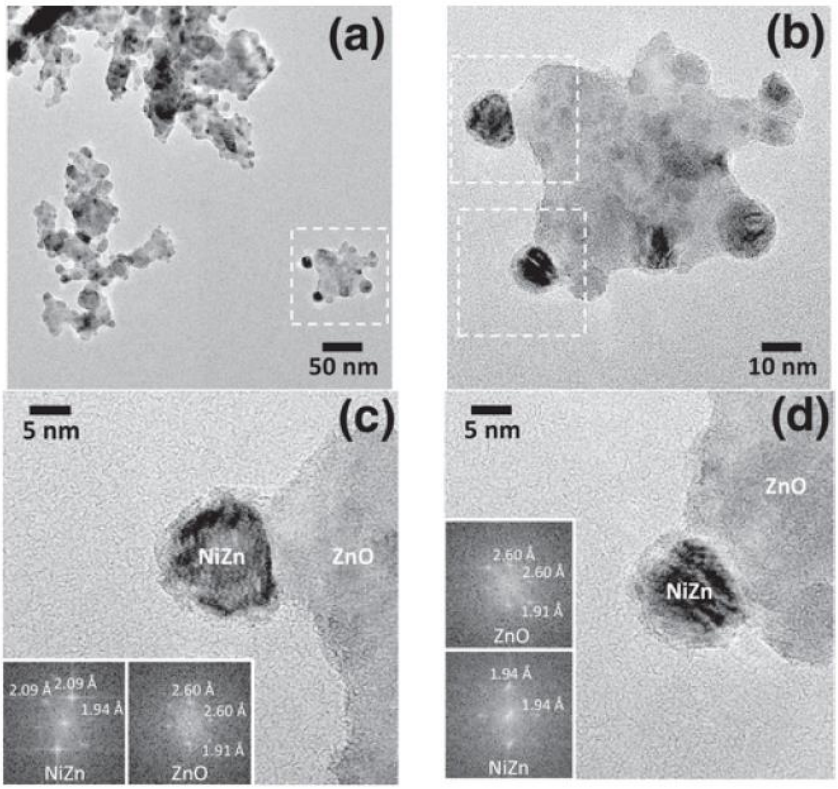
(a)
50 nm
(b)
10 nm
5 nm
(c)
NiZn
ZnO
2.09 Å
2.09 Å
1.94 Å
NiZn
2.60 Å
2.60 Å
1.91 Å
ZnO
5 nm
(d)
ZnO
NiZn
2.60 Å
2.60 Å
1.91 Å
ZnO
1.94 Å
1.94 Å
NiZn

Figure 6

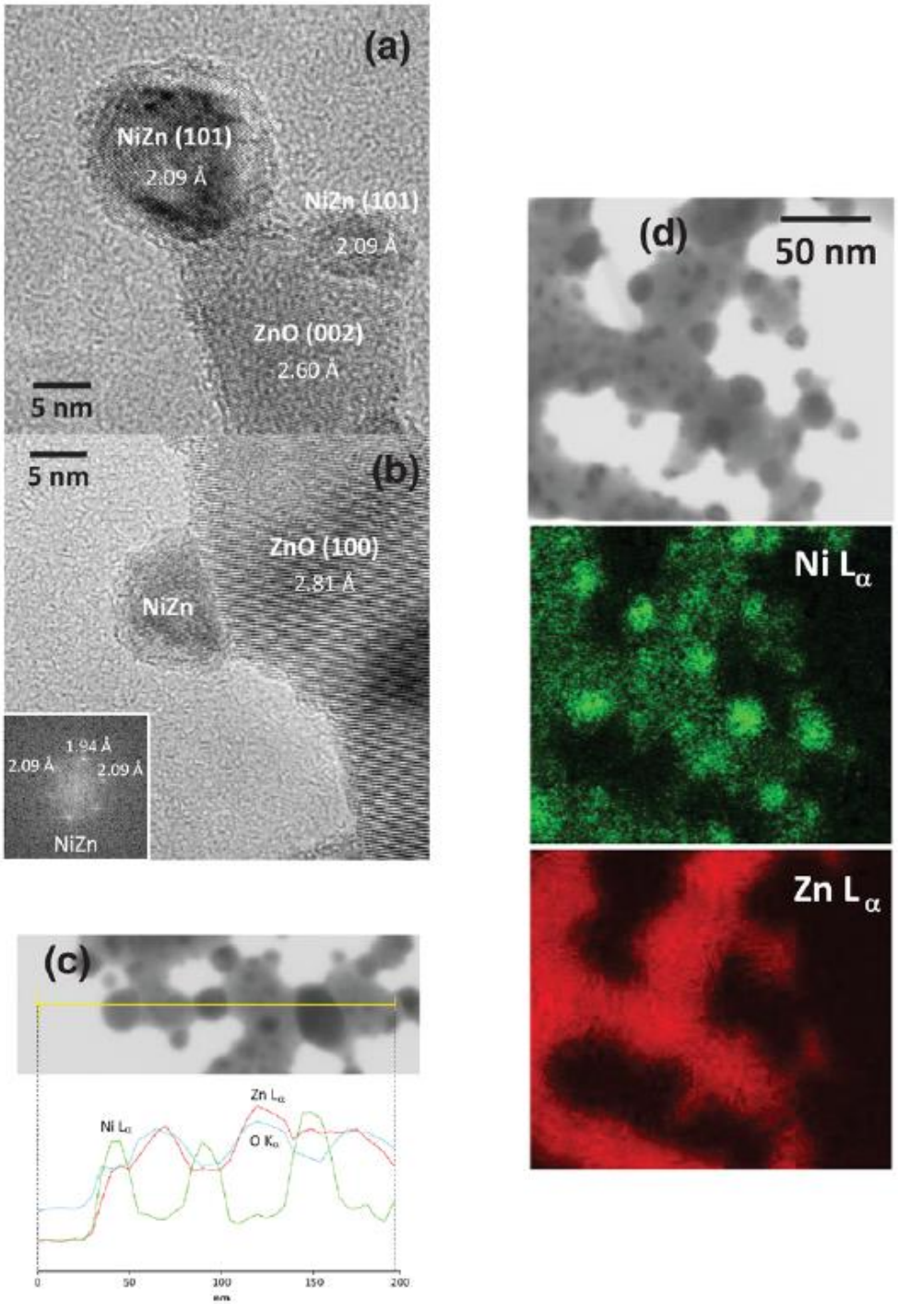
(a)
NiZn (101)
2.09 Å
NiZn (101)
2.09 Å
ZnO (002)
2.60 Å
5 nm
5 nm
(b)
ZnO (100)
2.81 Å
NiZn
1.94 Å
2.09 Å
2.09 Å
NiZn
(c)
Zn Lα
Ni Lα
O Kα
0
50
100
150
200
(d)
50 nm
Ni Lα
Zn Lα

Figure 7

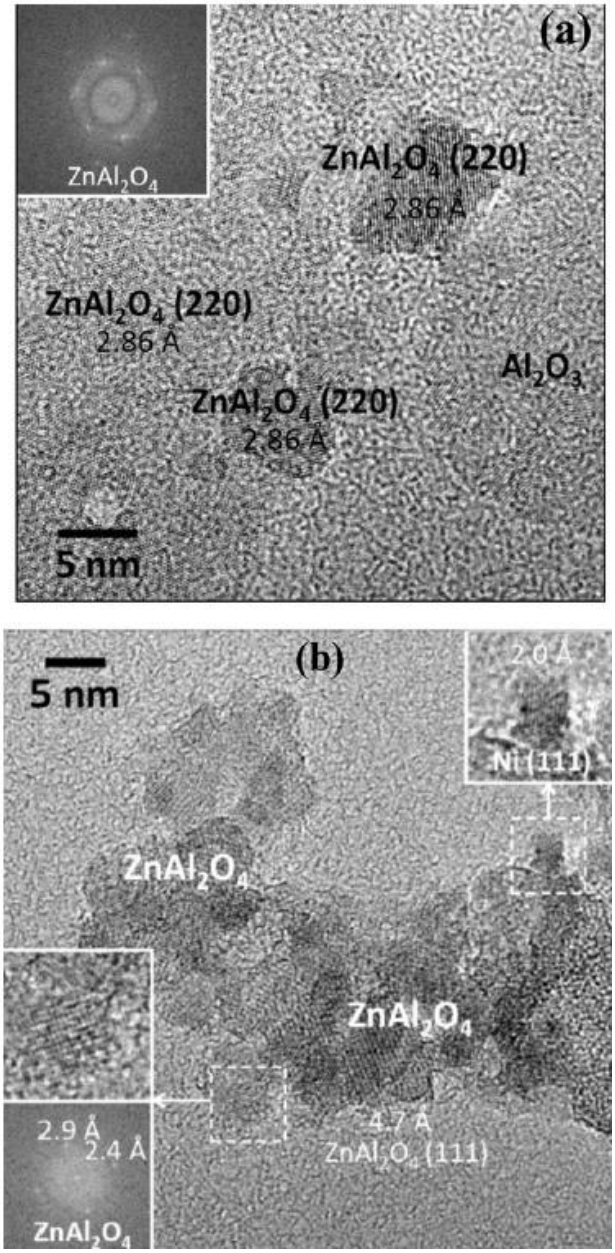
(a)
ZnAl2O4
ZnAl2O4 (220)
2.86 Å
ZnAl2O4 (220)
2.86 Å
Al2O3
ZnAl2O4 (220)
2.86 Å
5 nm
(b)
5 nm
2.0 Å
Ni (111)
ZnAl2O4
ZnAl2O4
2.9 Å
2.4 Å
ZnAl2O4
4.7 Å
ZnAl2O4 (111)

Figure 8

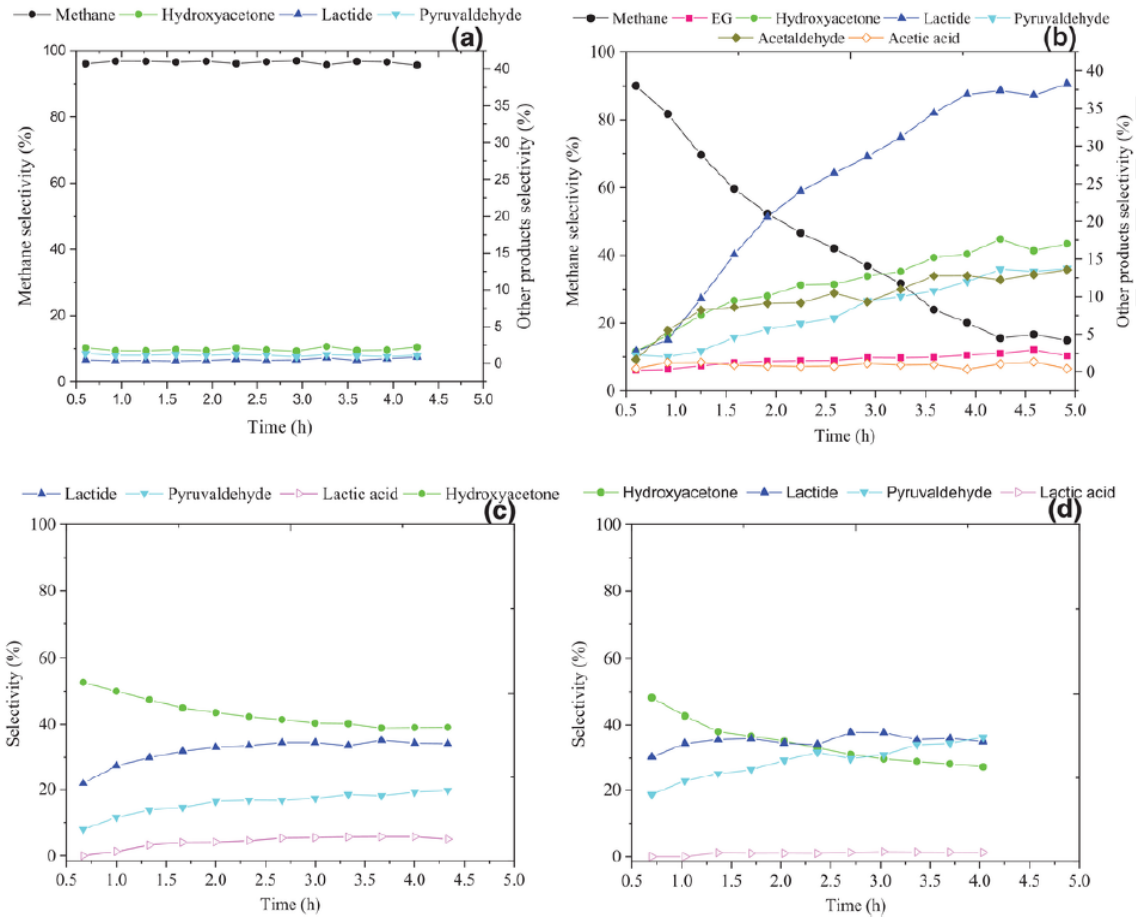

Figure 9

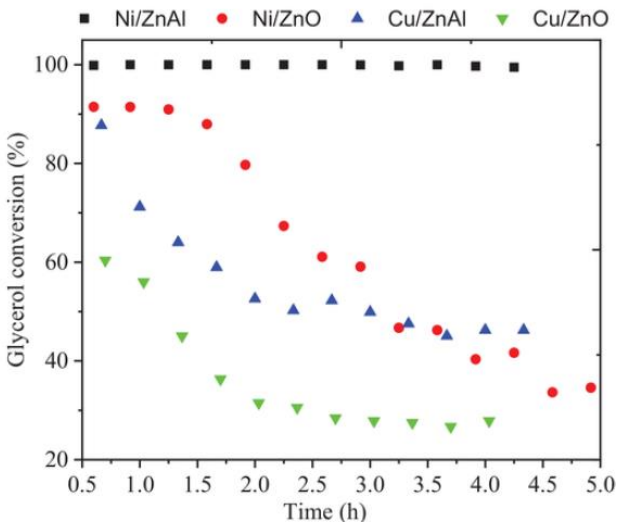

Scheme 1

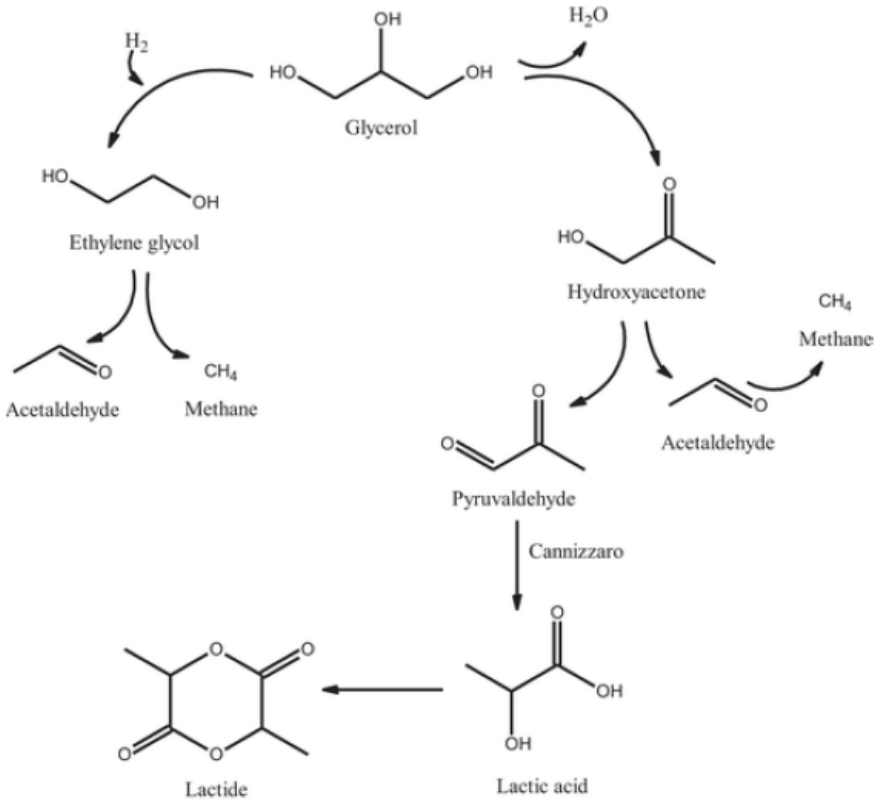
H2
OH
HO
OH
Glycerol
H2O
HO
OH
Ethylene glycol
O
HO
Hydroxyacetone
CH4
Methane
O
Acetaldehyde
CH4
Methane
O
Acetaldehyde
O
O
Pyruvaldehyde
Cannizzaro
O
OH
OH
Lactic acid
O
O
O
O
Lactide